Electronic Supplementary Information (ESI)

Quantum States of the Endohedral Fullerene $Li^+@C_{60}$ Surrounded by Anions: Energy Decomposition Analysis of Nuclear Wave Functions

Hideo Ando[1, a)] and Yoshihide Nakao[2]

[1)] *Faculty of Science, Yamagata University, 1-4-12 Kojirakawa-machi, Yamagata, Yamagata 990-8560, Japan.*

[2)] *Faculty of Life Science, Kyushu Sangyo University, 2-3-1 Matsukadai, Higashi-ku, Fukuoka 813-8503, Japan.*

(Dated: 4 March 2021)

Contents

[a)] Author to whom correspondence should be addressed. Electronic mail: ando@sci.kj.yamagata-u.ac.jp

Table S1. Position of every ring center. The distance from the polar z axis ($d_{\text{ring-}z}$) and the inclination angle from the z axis (θ_{ring}). See Fig. S1 for the terminologies of the ring centers.

	$d_{\text{ring-}z}$ (Å)	θ_{ring} (deg.)
$C_6(1)$	0.0000	0.00 or 180.00
$C_6(2)$	2.1596	41.77 or 138.23
$C_6(3)$	3.0561	70.53 or 109.47
$C_6(4)$	3.0564	70.52 or 109.48
$C_5(1)$	2.0161	37.37 or 142.63
$C_5(2)$	3.2563	79.20 or 100.80

Table S2. Position of every C atom. Distance from the cage center (r_{C}) and the inclination angle from the z axis (θ_{C}). The ten r_{C} distances are sorted in descending order. See Fig. S1 for the terminologies of the C^j atoms.

	r_{C} (Å)	θ_{C} (Å)
C^1	3.5452	23.65 or 156.35
C^2	3.5449	23.64 or 156.36
C^9	3.5435	80.42 or 99.58
C^3	3.5428	57.77 or 122.23
C^6	3.5414	47.19 or 132.81
C^4	3.5408	47.20 or 132.80
C^{10}	3.5381	85.97 or 94.03
C^8	3.5368	85.97 or 94.03
C^7	3.5333	63.07 or 116.93
C^5	3.5316	63.08 or 116.92

Details of the model energy functions for Eqs. (10)–(12)

We detail the functional forms for $V_{\rm es}(x,y,z)$, $V_{\rm es+exrep}(x,y,z)$, and $V_{\rm es+exrep+pol}(x,y,z)$ and summarize the fitting results. We first discuss the fitting for $V_{\rm es}(x,y,z)$ in Eq. (10). Figure 3a displays the electrostatic energies $\Delta E_{\rm es}$ (symbols) evaluated along the C_6 and C_5 rays (see Fig. S5 for the other radial rays and Fig. S11 for the polar plot). Along every C_6 ray, there exists a shallow energy minimum in a range of $r = 1.4$ to 1.5 Å, specifically, near a potential well of $V_{\rm es+exrep+pol+disp}$. Along every C_5 ray, in contrast, $\Delta E_{\rm es}$ exhibits an even shallower energy minimum around $r = 1.0$ Å and becomes repulsive as Li^+ further approaches the ring ($r > 1.3$ Å). It turns out that the $\Delta E_{\rm es}(x,y,z)$ grid data are reproduced by the modified Morse function in which the interaction points are assigned to the C=C and C−C centers, rather than to the C atoms.

$$
\begin{aligned}
&V_{\rm es}(x,y,z) \\
&= \sum_{j=1}^{15}\sum_{k=1}^{6}\left\{ D_e^j \left(\frac{\exp\left[2\alpha_e^j s_e^j (1-(s_k^j/s_e^j)^\zeta)/\zeta\right] - 2\exp\left[\alpha_e^j s_e^j (1-(s_k^j/s_e^j)^\zeta)/\zeta\right] - A^j}{1+A^j} \right) \right. \\
&\left. + V_{\rm shift} \right\},
\end{aligned}
\tag{S1}
$$

where s_k^j is the distance between Li^+ and a bond center, not the interatomic distance defined by Eq. (4). The index j and the index k run up to fifteen and six, respectively. This is because there are fifteen representative points at bond centers (i.e., five C=C centers and ten C−C centers), each of which has five more equivalent points. The optimized parameters are shown in Table S5. The average Morse parameter D_e for the C−C centers is 2.34 kcal/mol, and that for the C=C centers is 6.09 kcal/mol. The small D_e values for the C−C centers reflect the almost repulsive feature of $\Delta E_{\rm es}$ underneath the C_5 rings, which are composed of only C−C bonds. The large D_e values for the C=C centers reflect the stabilization of $\Delta E_{\rm es}$ underneath the C_6 rings, which include C=C bonds. The model function $V_{\rm es}(x,y,z)$ fits the $\Delta E_{\rm es}(x,y,z)$ grid data with an RMSE of 0.059 kcal/mol (Table S3). Even when recalculating the RMSE value by considering all of the grid points whose RI-MP2 energies are below −3.0 kcal/mol, the error remains small (0.127 kcal/mol). At the cage center, the model function $V_{\rm es}(x,y,z)$ approaches zero (0.382 kcal/mol). The radial and polar plots of $V_{\rm es}(x,y,z)$ are similar to those of the $\Delta E_{\rm es}(x,y,z)$

grid data (Figs. S5 and S11). Further characterization of $\Delta E_{\rm es}(x,y,z)$ and $V_{\rm es}(x,y,z)$ is presented in Sec. III C. We next discuss the fitting for $V_{\rm es+exrep}(x,y,z)$ in Eq. (11). Figure S6 displays the single-point energies of $\Delta E_{\rm es} + \Delta E_{\rm exrep}$ (symbols) along the 31 radial rays. As Li^+ approaches the C_{60} cage, the energy is significantly destabilized due to the purely repulsive nature of the exchange repulsion interaction, which is discussed in Sec. III C. The energy profiles along the C_5 rays are as repulsive as those along the C atom rays (Fig. S6a and b). We found that the $\Delta E_{\rm es}(x,y,z) + \Delta E_{\rm exrep}(x,y,z)$ grid data are reproduced by the sum of anti-Morse pair potentials,

$$\begin{aligned} &V_{\rm es+exrep}(x,y,z) \\ &= \sum_{j=1}^{12}\sum_{k=1}^{6}\left\{D_e^j\left(\exp\left[-2\alpha_e^j(s_k^j - s_e^j)\right] + 2\exp\left[-\alpha_e^j(s_k^j - s_e^j)\right]\right) + V_{\rm shift}\right\}, \end{aligned} \tag{S2}$$

where the interaction points are assigned to the C atoms and also to the $C_5(1)$ and $C_5(2)$ centers. Among the deposited interaction points are twelve representative points, each of which has five more equivalent points. The distance between Li^+ and every interaction point, s_k^j, is defined accordingly. The interaction points at the C_5 centers are the dummy sites empirically added to better reproduce the above-mentioned repulsive nature of $\Delta E_{\rm es} + \Delta E_{\rm exrep}$ underneath the C_5 centers. The optimized Morse parameters α_e for the C_5 centers are smaller than those for the C atoms (Table S6), which indicates that the dummy sites modify, in particular, the long-range energy profile underneath the C_5 rings. The RMSE value is 0.080 kcal/mol (Table S3). When considering all of the grid points whose RI-MP2 energies are below -3.0 kcal/mol, we found that the RMSE value remains small (0.389 kcal/mol). At the cage center, the model function $V_{\rm es+exrep}(x,y,z)$ approaches zero (-1.253 kcal/mol). The radial and polar plots of $V_{\rm es+exrep}(x,y,z)$ are similar to those of the $\Delta E_{\rm es}(x,y,z) + \Delta E_{\rm exrep}(x,y,z)$ grid data (Figs. S6 and S12). As shown in the row labeled $V_{\rm es+exrep}$ in Table 1, the model function reproduces the relative stabilities in $\Delta E_{\rm es} + \Delta E_{\rm exrep}$ underneath the individual ring centers at $r = 1.375$ Å. We finally discuss the fitting for $V_{\rm es+exrep+pol}(x,y,z)$ in Eq. (12). As is obvious from Eq. (6), $V_{\rm es+exrep+pol}(x,y,z)$ is a model function of the RHF potential energy surface. Because the overall profile of the RHF potential energy surface (Figs. S7 and S13) is similar to that of the RI-MP2 one (Figs. S2 and S4), we employed a function similar to $V_{\rm es+exrep+pol+disp}(x,y,z)$ in Eq. (2). To reproduce the RHF energies, $\Delta E_{\rm es}(x,y,z) + \Delta E_{\rm exrep}(x,y,z) + \Delta E_{\rm pol}(x,y,z)$, evaluated at

the grid points, we again deposited dummy interaction points at the $C_5(1)$ and $C_5(2)$ centers in addition to the interaction points at the C atoms.

$$
\begin{aligned}
& V_{\mathrm{es+exrep+pol}}(x,y,z) \\
&= \sum_{j=1}^{12}\sum_{k=1}^{6}\Bigg\{ D_e^j \left(\frac{\exp\left[2\alpha_e^j s_e^j (1-(s_k^j/s_e^j)^\zeta)/\zeta\right] - 2\exp\left[\alpha_e^j s_e^j (1-(s_k^j/s_e^j)^\zeta)/\zeta\right] - A^j}{1+A^j} \right) \\
&+ V_{\mathrm{shift}} \Bigg\}. \qquad \text{(S3)}
\end{aligned}
$$

The optimized parameters for the C atoms, listed in Table S7, are close to those of $V_{\mathrm{es+exrep+pol+disp}}(x,y,z)$ in Table S4. The optimized Li^+−$C_5(1)$ and Li^+−$C_5(2)$ pair potentials describe the repulsive energy profile underneath the C_5 rings. The RMSE value is 0.073 kcal/mol (Table S3). The RMSE value recalculated using all of the grid points whose RI-MP2 energies are below −3.0 kcal/mol remains small (0.325 kcal/mol). At the cage center, the model function $V_{\mathrm{es+exrep+pol}}(x,y,z)$ approaches zero (−0.807 kcal/mol). As shown in Figs. S7 and S13, the radial and polar plots of $V_{\mathrm{es+exrep+pol}}(x,y,z)$ are similar to those of the grid data of $\Delta E_{\mathrm{es}}(x,y,z) + \Delta E_{\mathrm{exrep}}(x,y,z) + \Delta E_{\mathrm{pol}}(x,y,z)$. As shown in the row labeled $V_{\mathrm{es+exrep+pol}}$ in Table 1, the model function reproduces the relative stabilities in $\Delta E_{\mathrm{es}} + \Delta E_{\mathrm{exrep}} + \Delta E_{\mathrm{pol}}$ underneath the individual ring centers at $r = 1.375$ Å.

Table S3. Energies at the C_{60} cage center and the root-mean-square errors (RMSEs) of the model functions. All values are given in kcal/mol. The optimized model parameters are tabulated in Tables S4–S7.

	V_{es}	$V_{\mathrm{es+exrep}}$	$V_{\mathrm{es+exrep+pol}}$	$V_{\mathrm{es+exrep+pol+disp}}$
Model	modified Morse	anti-Morse	modified Morse	modified Morse
Energy at the cage center	0.38198	−1.25267	−0.80691	−0.78462
RMSE (−7.0 kcal/mol)	0.05922	0.07982	0.07297	0.05667
RMSE (−5.0 kcal/mol)[a]	0.09860	0.28233	0.25640	0.15486
RMSE (−3.0 kcal/mol)[a]	0.12747	0.38897	0.32531	0.23822
RMSE (0.0 kcal/mol)[a]	0.24452	1.11148	0.99948	0.63441
		V_{exrep}	V_{pol}	V_{disp}
RMSE (−7.0 kcal/mol)		0.12735	0.01167	0.03042

[a] Remember that only the grid point data whose RI-MP2 energies are below an energy threshold of −7.0 kcal/mol were considered in our Levenberg–Marquardt fitting procedures. The RMSEs shown here are the RMSEs evaluated using more grid point data, without modifying the model functions. For example, RMSE (0.0 kcal/mol) was evaluated using all of the grid point data whose RI-MP2 energies are below 0.0 kcal/mol, which include grid point data ignored in the model fitting (e.g., the cage center). They are an index of the reliability of the model function in the high-energy region.

Table S4. Modified Morse parameters for RI-MP2 potential energy surface, $V_{\mathrm{es+exrep+pol+disp}}$ in Eq. (2).

	D_e^j (kcal/mol)	α_e^j (Å^{-1})	s_e^j (Å)
C^1 $(j=1)$[a]	11.087429950	1.351701280	2.145309009
C^2 $(j=2)$	11.094227140	1.360299848	2.142729060
C^3 $(j=3)$	10.854120581	1.307030861	2.159534192
C^4 $(j=4)$	12.742252317	1.379406321	2.116788829
C^5 $(j=5)$	12.402919188	1.300671377	2.153606371
C^6 $(j=6)$	12.700338579	1.380025096	2.117645180
C^7 $(j=7)$	12.254425101	1.304014740	2.154503104
C^8 $(j=8)$	10.501678909	1.435033605	2.147589193
C^9 $(j=9)$	10.273065558	1.480098217	2.136909921
C^{10} $(j=10)$	10.523702664	1.442765493	2.146237653
	V_{shift} (kcal/mol)	ζ	
	5.443241303	−0.666295116	

[a] See Fig. S1 for the positions of the C^j atoms.

Table S5. Modified Morse parameters for $V_{\rm es}$ in Eq. (S1).

	D_e^j (kcal/mol)	α_e^j (Å^{-1})	s_e^j (Å)
C^1=C^2 $(j=1)$[a]	6.346133479	4.410124525	1.481258372
C^4=C^5 $(j=2)$	6.097745804	4.473701937	1.496650836
C^6=C^7 $(j=3)$	6.108790649	4.467224470	1.496435531
C^8=C^{10} $(j=4)$	6.015696608	4.673375432	1.484776840
C^3=C^9 $(j=5)$	5.878370218	4.810533143	1.523178793
C^1−C^6 $(j=6)$[a]	2.238391468	0.832115727	2.131350063
C^2−C^4 $(j=7)$	2.239539903	0.832519443	2.132327818
C^3−C^4 $(j=8)$	1.859599568	0.666679130	2.281324574
C^5−C^7 $(j=9)$	2.841170388	0.657446165	2.153084939
C^5−C^8 $(j=10)$	2.719004672	0.778657391	2.107423396
C^7−C^{10} $(j=11)$	2.721380628	0.799628575	2.096971917
C^8−C^9 $(j=12)$	2.215825538	0.545518518	2.281275745
C^9−C^{10} $(j=13)$	2.186898895	0.522413020	2.303638605
C^1−C^2 $(j=14)$	2.473373852	0.618112383	2.257521534
C^3−C^6 $(j=15)$	1.889002082	0.684360024	2.266405015
	$V_{\rm shift}$ (kcal/mol)	ζ	
	1.127800496	−1.253298833	

[a] The 6:6 ring bonds (between two C_6 rings) are designated by double bonds, and the 6:5 ring bonds (between a C_6 ring and a C_5 ring) are designated by single bonds. See Fig. S1 for the positions of the C^j atoms.

Table S6. Anti-Morse parameters for $V_{\mathrm{es+exrep}}$ in Eq. (S2).

	D_e^j (kcal/mol)	α_e^j (Å^{-1})	s_e^j (Å)
C^1 $(j=1)$[a]	2.197160258	3.457781655	2.019605749
C^2 $(j=2)$	2.521262908	3.318355817	2.004866916
C^3 $(j=3)$	3.679342666	3.216069586	1.934556747
C^4 $(j=4)$	3.209700186	3.366871027	1.953027816
C^5 $(j=5)$	2.132755607	3.889430461	2.006113553
C^6 $(j=6)$	3.508143546	3.333154677	1.939421862
C^7 $(j=7)$	1.890634962	4.003419068	2.019948108
C^8 $(j=8)$	2.763247765	3.646054428	1.975144578
C^9 $(j=9)$	1.881202626	3.955459322	2.021436127
C^{10} $(j=10)$	2.924582204	3.622855410	1.967385085
$C_5(1)$ $(j=11)$[b]	2.010920538	0.295531242	2.009804263
$C_5(2)$ $(j=12)$	0.035572802	0.861651181	4.711354303
	V_{shift} (kcal/mol)		
	−0.393612760		

[a] See Fig. S1 for the positions of the C^j atoms.

[b] See Fig. S1 for the positions of the C_5 ring centers.

Table S7. Modified Morse parameters for the RHF potential energy surface, $V_{\mathrm{es+exrep+pol}}$ in Eq. (S3).

	D_e^j (kcal/mol)	α_e^j (Å^{-1})	s_e^j (Å)
C^1 $(j=1)$[a]	10.569018375	1.194048692	2.154599137
C^2 $(j=2)$	10.574713862	1.166758605	2.159820432
C^3 $(j=3)$	10.575479979	1.066773360	2.176329760
C^4 $(j=4)$	12.445410921	1.053929239	2.152801430
C^5 $(j=5)$	12.294740201	1.180258503	2.141883026
C^6 $(j=6)$	12.407956853	1.031745416	2.159176464
C^7 $(j=7)$	12.147928777	1.218658814	2.138006264
C^8 $(j=8)$	10.354662698	1.183556310	2.163699964
C^9 $(j=9)$	10.121220417	1.490625121	2.126476720
C^{10} $(j=10)$	10.376195932	1.174007750	2.165921558
$C_5(1)$ $(j=11)$[b]	0.109149723	0.051447204	1.863405516
$C_5(2)$ $(j=12)$[b]	0.880947110	0.022752571	3.044255627
	V_{shift} (kcal/mol)	ζ	
	4.459123191	−1.575919288	

[a] See Fig. S1 for the positions of the C^j atoms.

[b] The optimized modified Morse potentials at the $C_5(1)$ and $C_5(2)$ centers have a repulsive feature. See Fig. S1 for the positions of the C_5 ring centers.

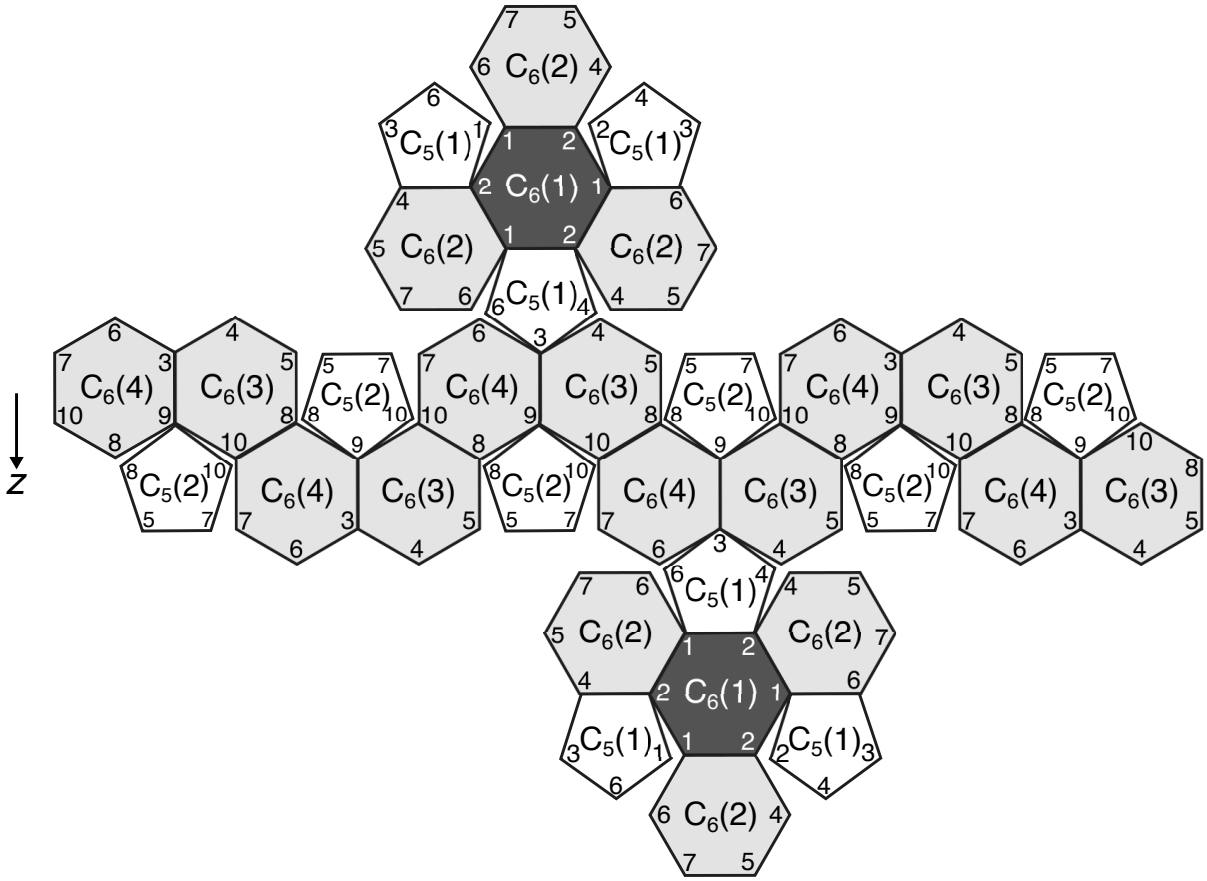

Fig. S1. Unwrapped and flattened map of the C_{60} cage in the $[Li^+@C_{60}]6PF_6^-$ model, and the terminologies of the important points on the cage surface. The C_{60} cage has the S_6 symmetry. Any two points denoted by the same terminology are symmetrically equivalent. For the carbon sites C^j ($j = 1, 2, \cdots, 10$), only the number j is shown. The two $C_6(1)$ rings are shown in dark gray, while the $C_6(2)$ rings and the $C_6(3)-C_6(4)$ zigzag band are shown in light gray. There is a single F atom in close contact with every $C_6(2)$ center. See Fig. 1 for the original geometry before unwrapping.

Note that in this paper, the chemical bond between two C_6 rings is designated by C=C double bond, and the bond between a C_5 ring and a C_6 ring is designated by C−C single bond, regardless of the actual electronic structure (e.g., bond order indices). Accordingly, every C_6 ring is composed of three C=C bonds and three C−C bonds, whereas every C_5 ring is composed of only C−C bonds.

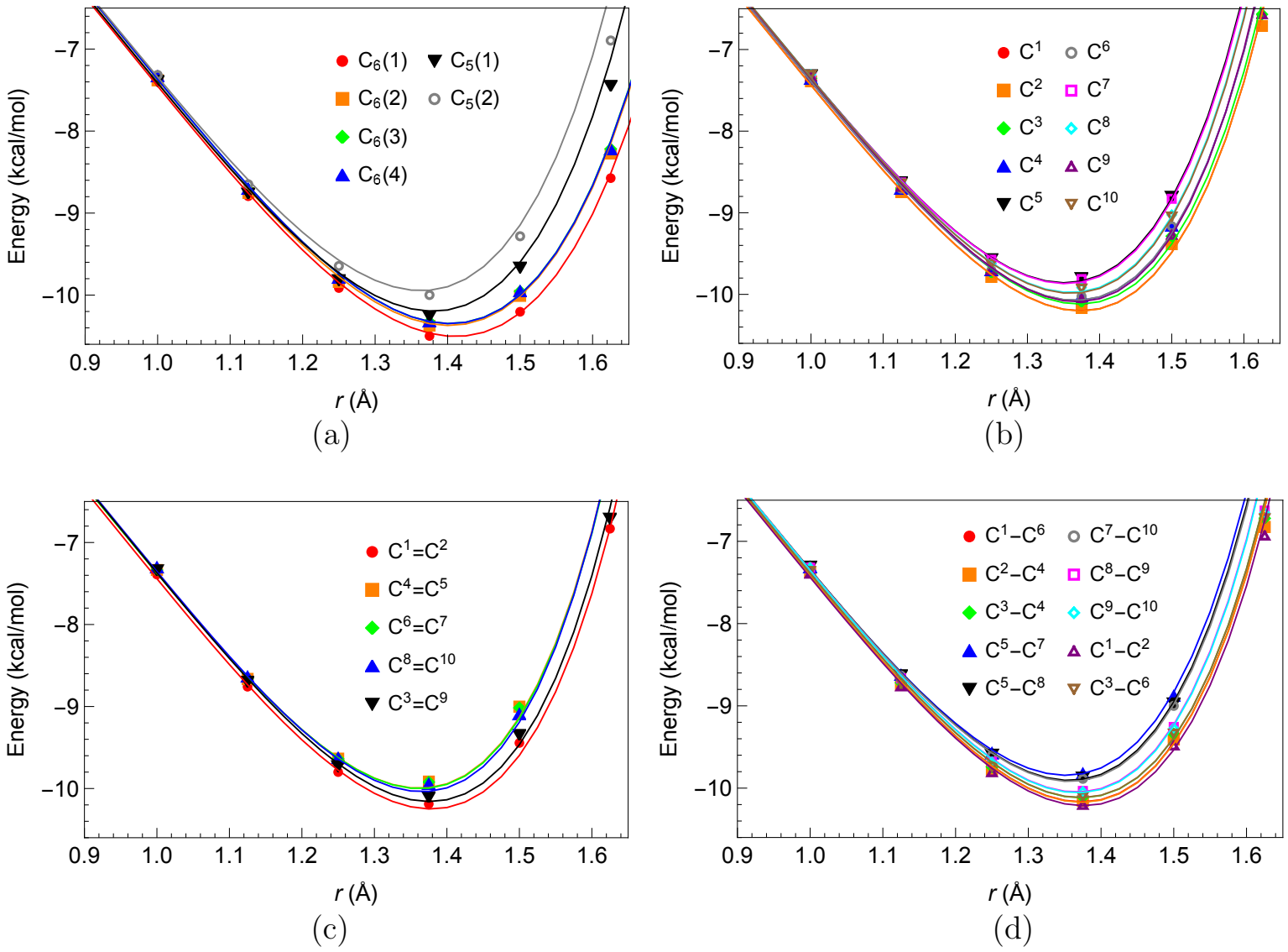

Fig. S2. Radial profiles of the RI-MP2 potential energy function $V_{\mathrm{es+exrep+pol+disp}}$ (curves) along the 31 one-dimensional rays: the rays toward (a) ring centers, (b) C atoms, (c) C=C bond centers, and (d) C−C bond centers. The symbols are the single-point calculation energies, $\Delta E_{\mathrm{RI\text{-}MP2}} = \Delta E_{\mathrm{es}} + \Delta E_{\mathrm{exrep}} + \Delta E_{\mathrm{pol}} + \Delta E_{\mathrm{disp}}$, which are relative to the energy at $r = 0$ Å.

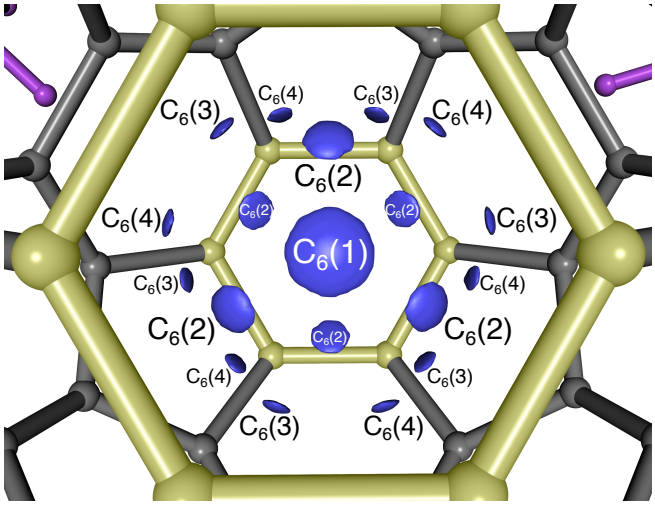

(a) Isovalue = −10.30 kcal/mol

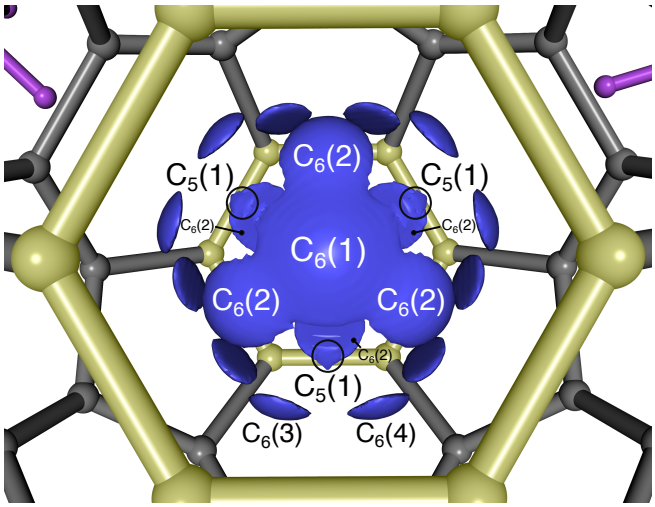

(b) Isovalue = −10.19 kcal/mol

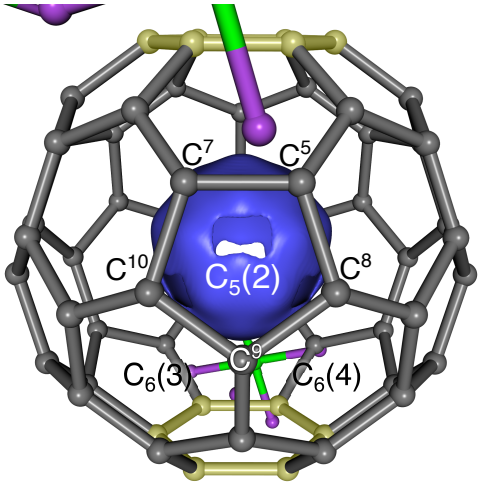

(c) Isovalue = −9.93 kcal/mol

Fig. S3. Isosurface plots of the model potential energy function $V_{\mathrm{es+exrep+pol+disp}}$: (a) top view with an isovalue of −10.30 kcal/mol, (b) top view with an isovalue of −10.19 kcal/mol, and (c) side view with an isovalue of −9.93 kcal/mol. The two $C_6(1)$ rings are indicated by the yellow highlights. See Fig. S1 for the unwrapped geometry of the cage. See the next page for the detailed explanation of this figure.

Regarding the isosurface plots of the model potential energy function

When using an isovalue of −10.30 kcal/mol (Fig. S3a), we found twenty islands, each of which corresponds to a deep C_6 potential well. In Fig. S3a, the rear island of one $C_6(1)$ well ($z < 0$) is hidden by the front island of the other $C_6(1)$ well ($z > 0$). Since the $C_6(1)$ wells are the deepest and the $C_6(2)$ wells are the second deepest, their islands are larger than the islands of the $C_6(3)$ and $C_6(4)$ wells. When the isovalue is increased to −10.19 kcal/mol (Fig. S3b), three tiny islands emerge next to each of the $C_6(1)$ islands. These correspond to the shallow $C_5(1)$ wells. When the isovalue is increased to −9.93 kcal/mol (Fig. S3c), a thin pseudo-spherical shell appears, as is expected based on the fact that all radial rays exhibit minima around $r = 1.375$ Å (Fig. S2). Underneath the C^5, C^7, C^8, and C^{10} atoms of every $C_5(2)$ ring, there is a U-shaped hole in the shell. Underneath a C^9 atom, in contrast, there is no hole in the shell. The thin shell includes the $C_6(3)$ and $C_6(4)$ wells and continuously extends below the C^9 atoms. This suggests that underneath a $C_5(2)$ ring, there is no distinct potential well that restricts the librational motion of Li^+ in the shell. This is consistent with our experience of preliminary DFT(M06-2X)/cc-pVDZ calculations. In the DFT geometry optimization using a standard convergence tolerance of Gaussian 09,[1] we found an equilibrium structure in which Li^+ is located almost directly underneath a $C_5(2)$ center, as mentioned in Sec. II. However, when we tried to further refine the structure using a tight convergence tolerance (Opt=Tight option in Gaussian 09),[1] Li^+ eventually moved to the neighboring $C_6(4)$ well.

[1] M. J. Frisch, G. W. Trucks, H. B. Schlegel, G. E. Scuseria, M. A. Robb, J. R. Cheeseman, G. Scalmani, V. Barone, B. Mennucci, G. A. Petersson, H. Nakatsuji, M. Caricato, X. Li, H. P. Hratchian, A. F. Izmaylov, J. Bloino, G. Zheng, J. L. Sonnenberg, M. Hada, M. Ehara, K. Toyota, R. Fukuda, J. Hasegawa, M. Ishida, T. Nakajima, Y. Honda, O. Kitao, H. Nakai, T. Vreven, J. A. Montgomery, Jr., J. E. Peralta, F. Ogliaro, M. Bearpark, J. J. Heyd, E. Brothers, K. N. Kudin, V. N. Staroverov, R. Kobayashi, J. Normand, K. Raghavachari, A. Rendell, J. C. Burant, S. S. Iyengar, J. Tomasi, M. Cossi, N. Rega, J. M. Millam, M. Klene, J. E. Knox, J. B. Cross, V. Bakken, C. Adamo, J. Jaramillo, R. Gomperts, R. E. Stratmann, O. Yazyev, A. J. Austin, R. Cammi, C. Pomelli, J. W. Ochterski, R. L. Martin, K. Morokuma, V. G. Zakrzewski, G. A. Voth, P. Salvador, J. J. Dannenberg, S. Dapprich, A. D. Daniels, Ö. Farkas, J. B. Foresman, J. V. Ortiz, J. Cioslowski and D. J. Fox, Gaussian 09 (Revision D.01), Gaussian, Inc., Wallingford CT, 2009.

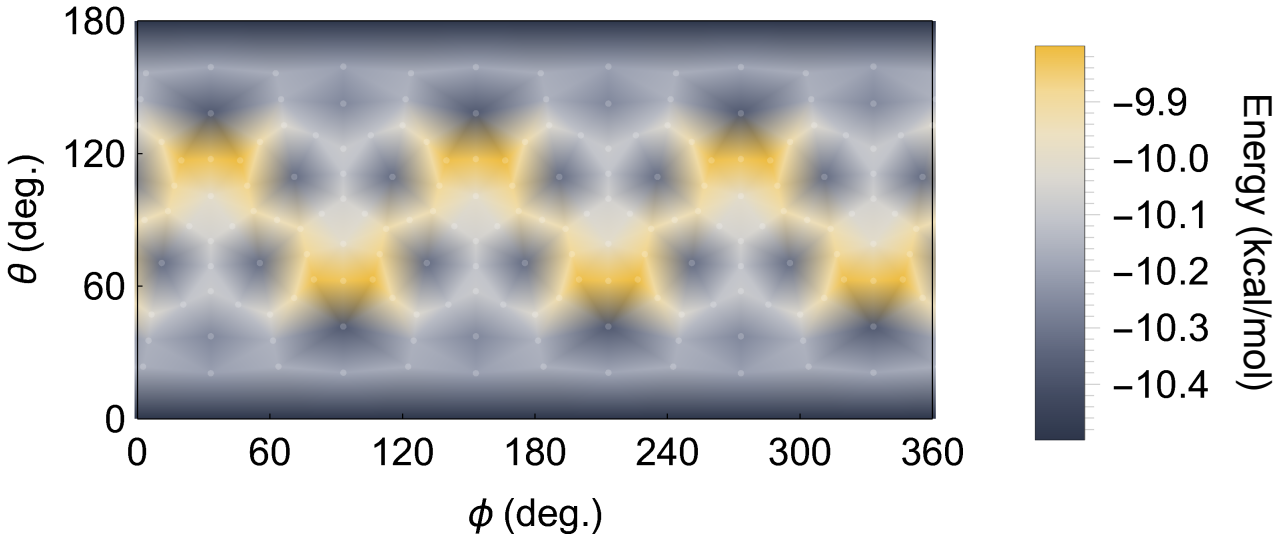

(a) Single-point calculation

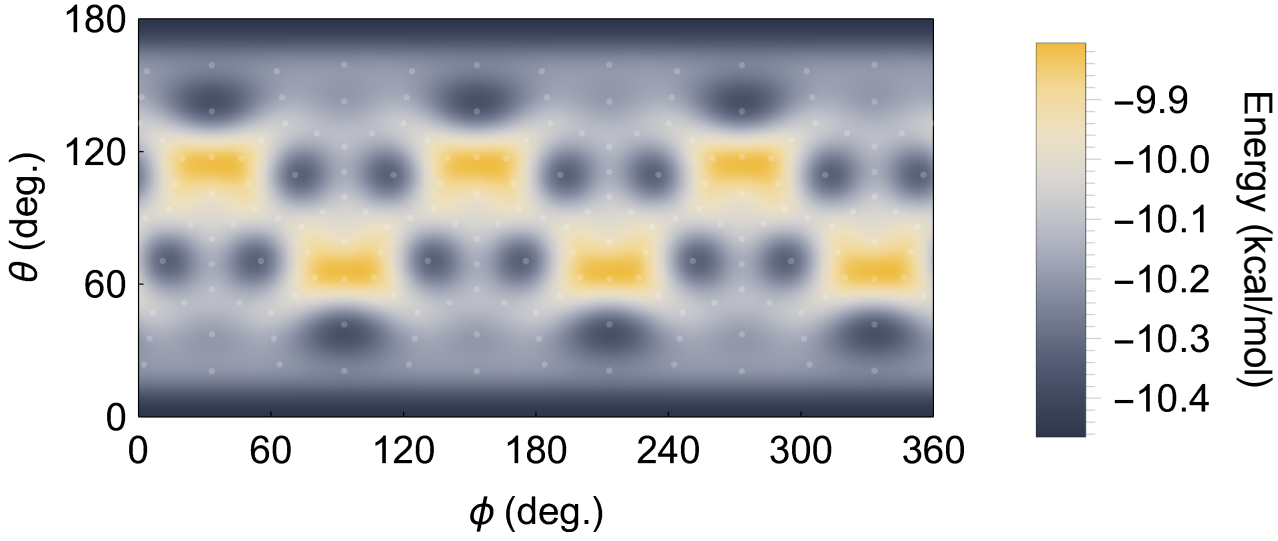

(b) Model function

Fig. S4. Polar plot of the RI-MP2 potential energy function in a spherical shell with $r = 1.375$ Å: (a) the single-point calculation data, $\Delta E_{\text{RI-MP2}} = \Delta E_{\text{es}} + \Delta E_{\text{exrep}} + \Delta E_{\text{pol}} + \Delta E_{\text{disp}}$, and (b) the model function $V_{\text{es+exrep+pol+disp}}$. The positions underneath the C atoms, bond centers, and ring centers, except those underneath the $C_6(1)$ centers at the two poles, are indicated by the semitransparent white points, at which single-point calculations were performed. The color map was generated by interpolating the data points by means of a Delaunay triangulation. The plot range, shown in the bar legend, was defined by using the minimum and maximum energies in the spherical shell with $r = 1.375$ Å.

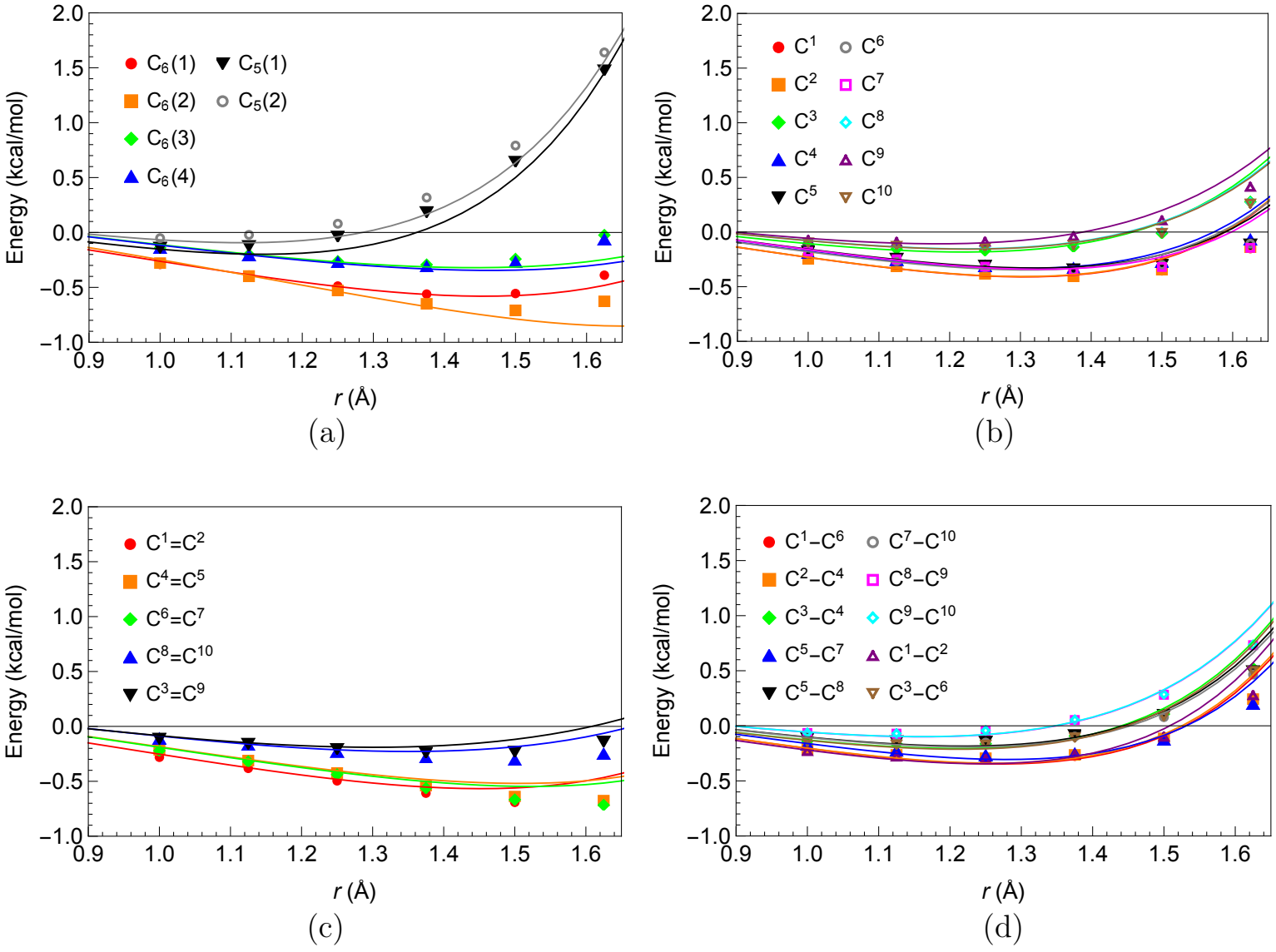

Fig. S5. Radial profiles of the electrostatic energy function V_{es} (curves) along the 31 one-dimensional rays: the rays toward (a) ring centers, (b) C atoms, (c) C=C bond centers, and (d) C−C bond centers. The symbols are the single-point calculation energies, ΔE_{es}, which are relative to the energy at $r = 0$ Å.

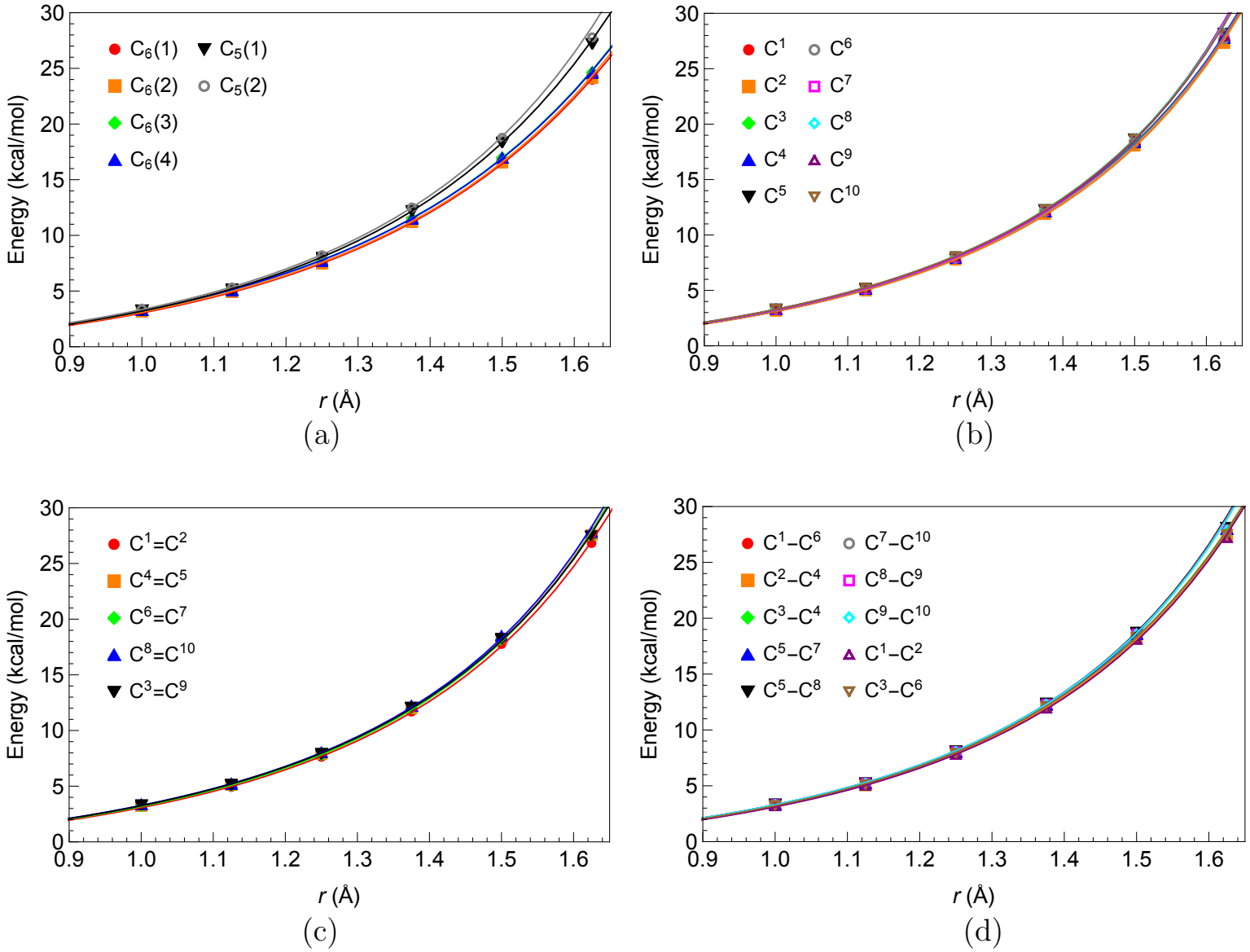

Fig. S6. Radial profiles of the decomposed energy function $V_{\mathrm{es+exrep}}$ (curves) along the 31 one-dimensional rays: the rays toward (a) ring centers, (b) C atoms, (c) C=C bond centers, and (d) C−C bond centers. The symbols are the single-point calculation energies, $\Delta E_{\mathrm{es}} + \Delta E_{\mathrm{exrep}}$, which are relative to the energy at $r = 0$ Å.

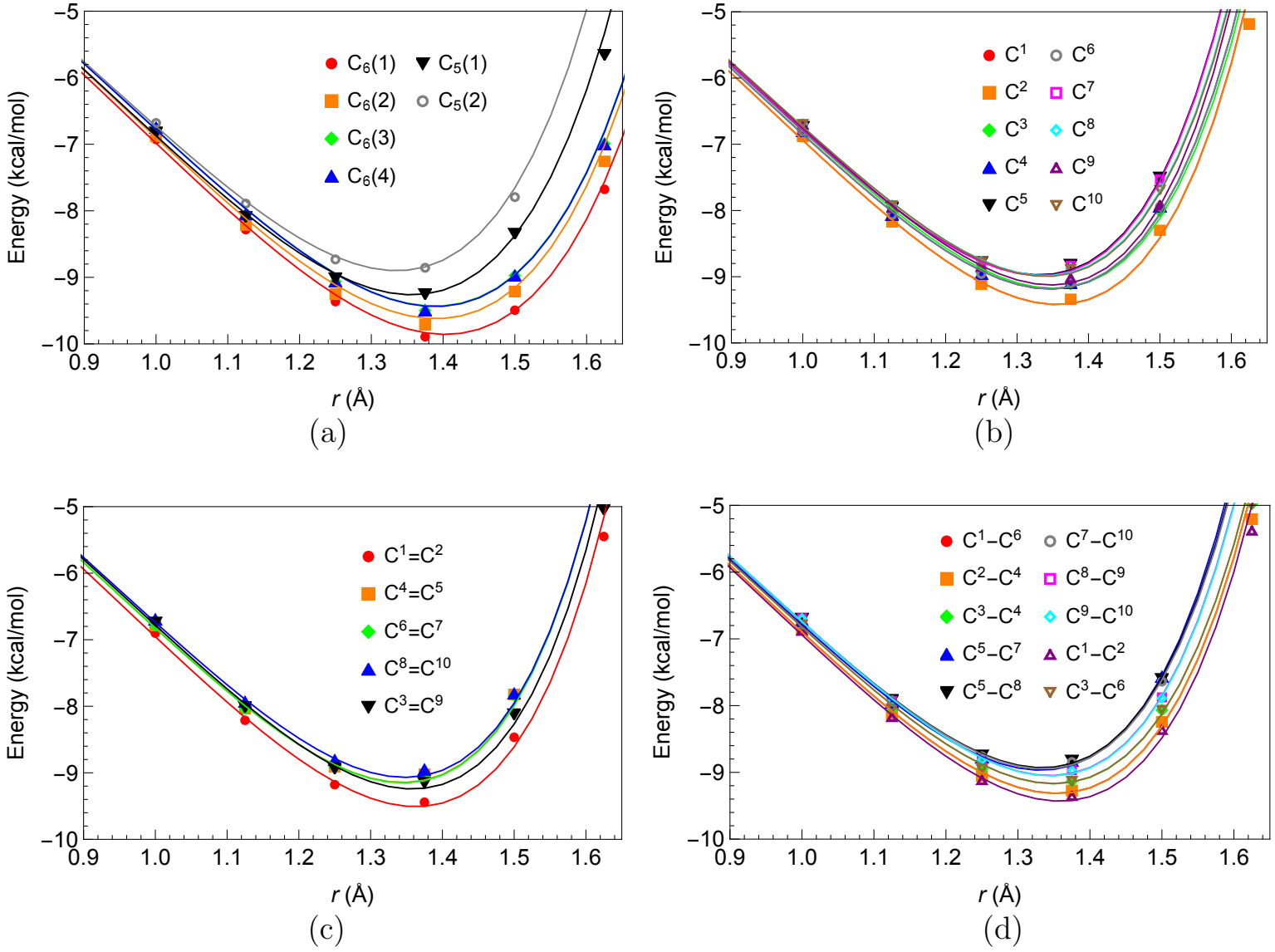

Fig. S7. Radial profiles of the RHF potential energy function $V_{\mathrm{es+exrep+pol}}$ (curves) along the 31 one-dimensional rays: the rays toward (a) ring centers, (b) C atoms, (c) C=C bond centers, and (d) C−C bond centers. The symbols are the single-point calculation energies, $\Delta E_{\mathrm{es}} + \Delta E_{\mathrm{exrep}} + \Delta E_{\mathrm{pol}}$, which are relative to the energy at $r = 0$ Å.

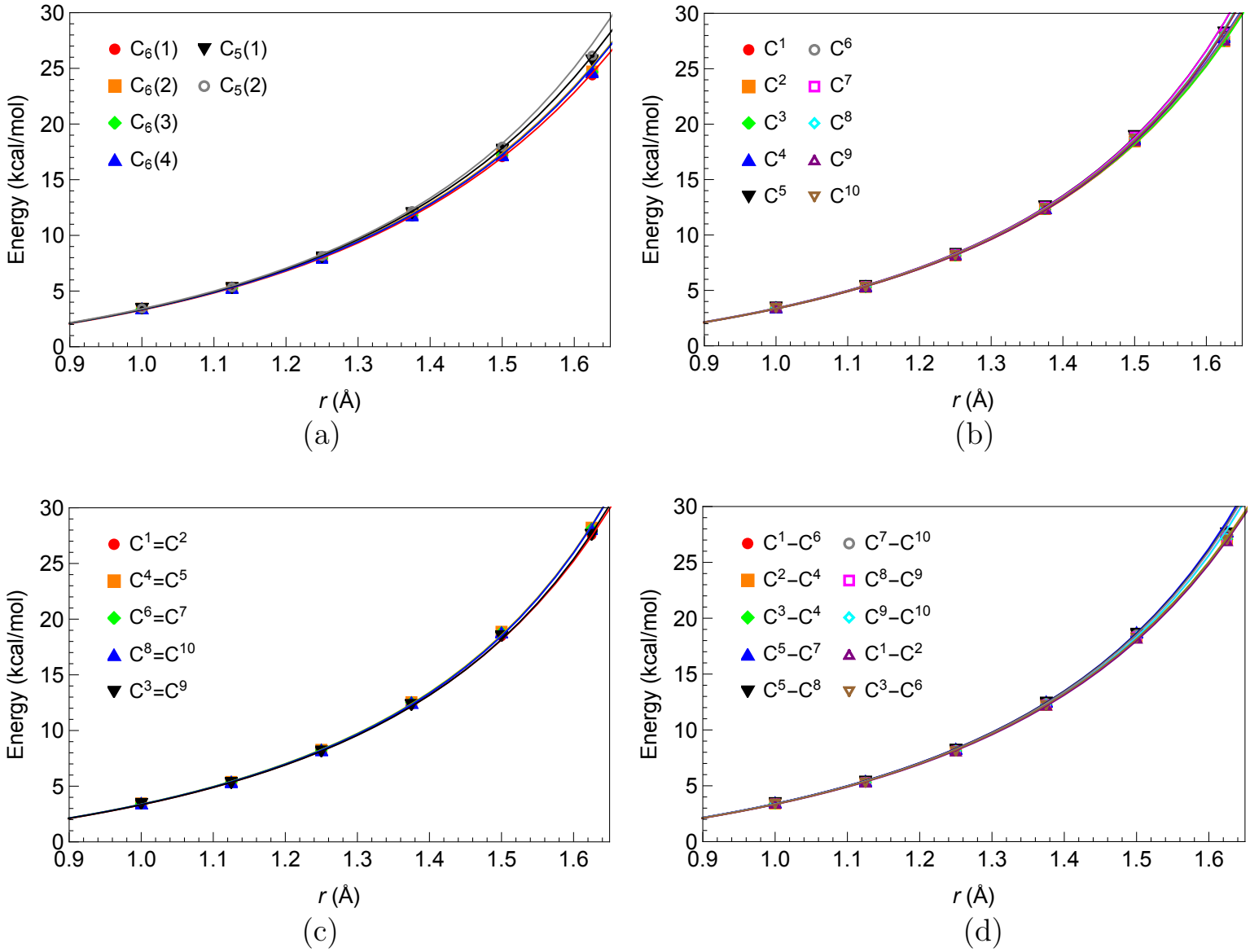

Fig. S8. Radial profiles of the exchange repulsion energy function V_{exrep} (curves) along the 31 one-dimensional rays: the rays toward (a) ring centers, (b) C atoms, (c) C=C bond centers, and (d) C−C bond centers. The symbols are the single-point calculation energies, $\Delta E_{\mathrm{exrep}}$, which are relative to the energy at $r = 0$ Å.

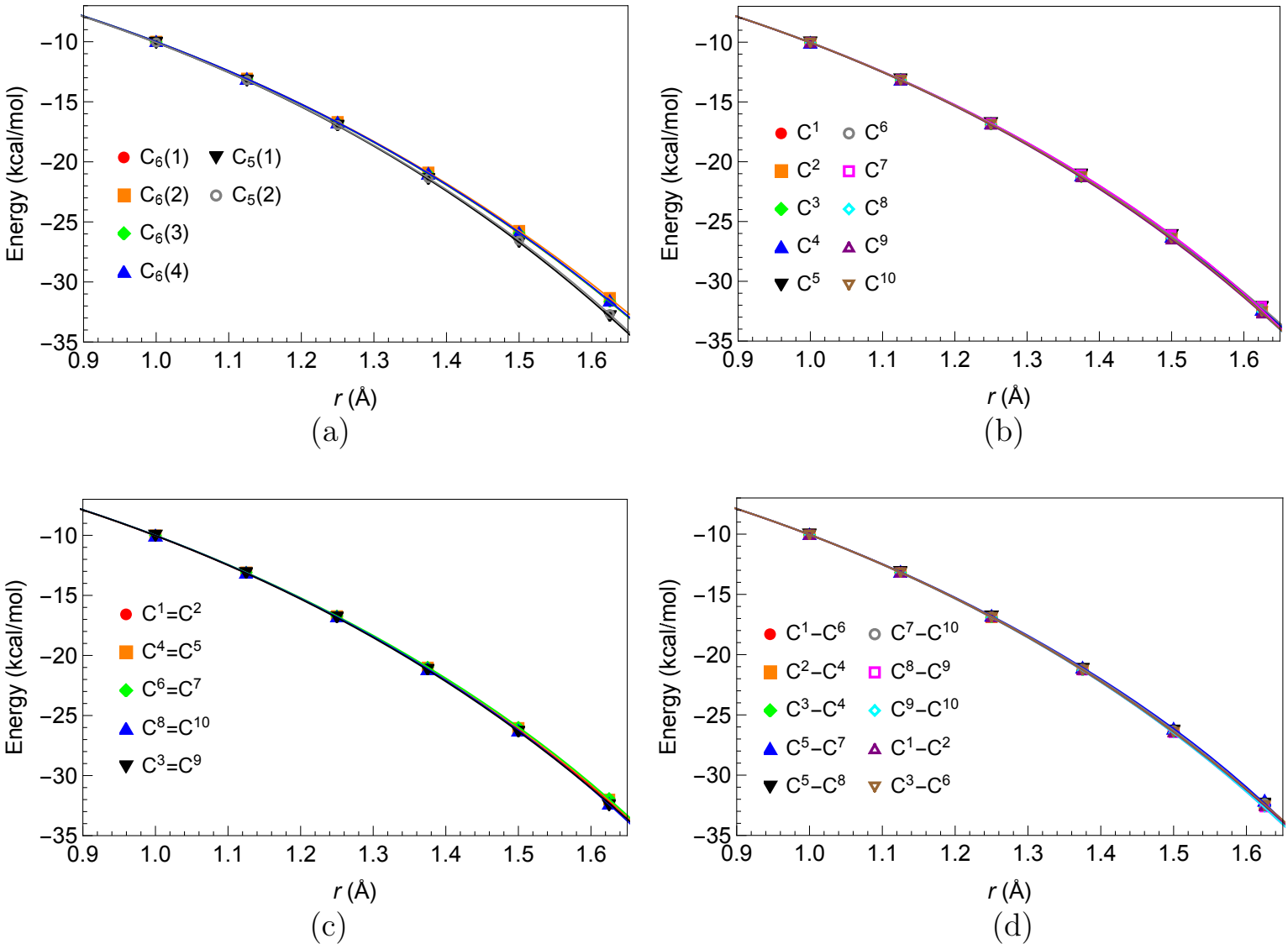

Fig. S9. Radial profiles of the polarization energy function V_{pol} (curves) along the 31 one-dimensional rays: the rays toward (a) ring centers, (b) C atoms, (c) C=C bond centers, and (d) C−C bond centers. The symbols are the single-point calculation energies, ΔE_{pol}, which are relative to the energy at $r = 0$ Å.

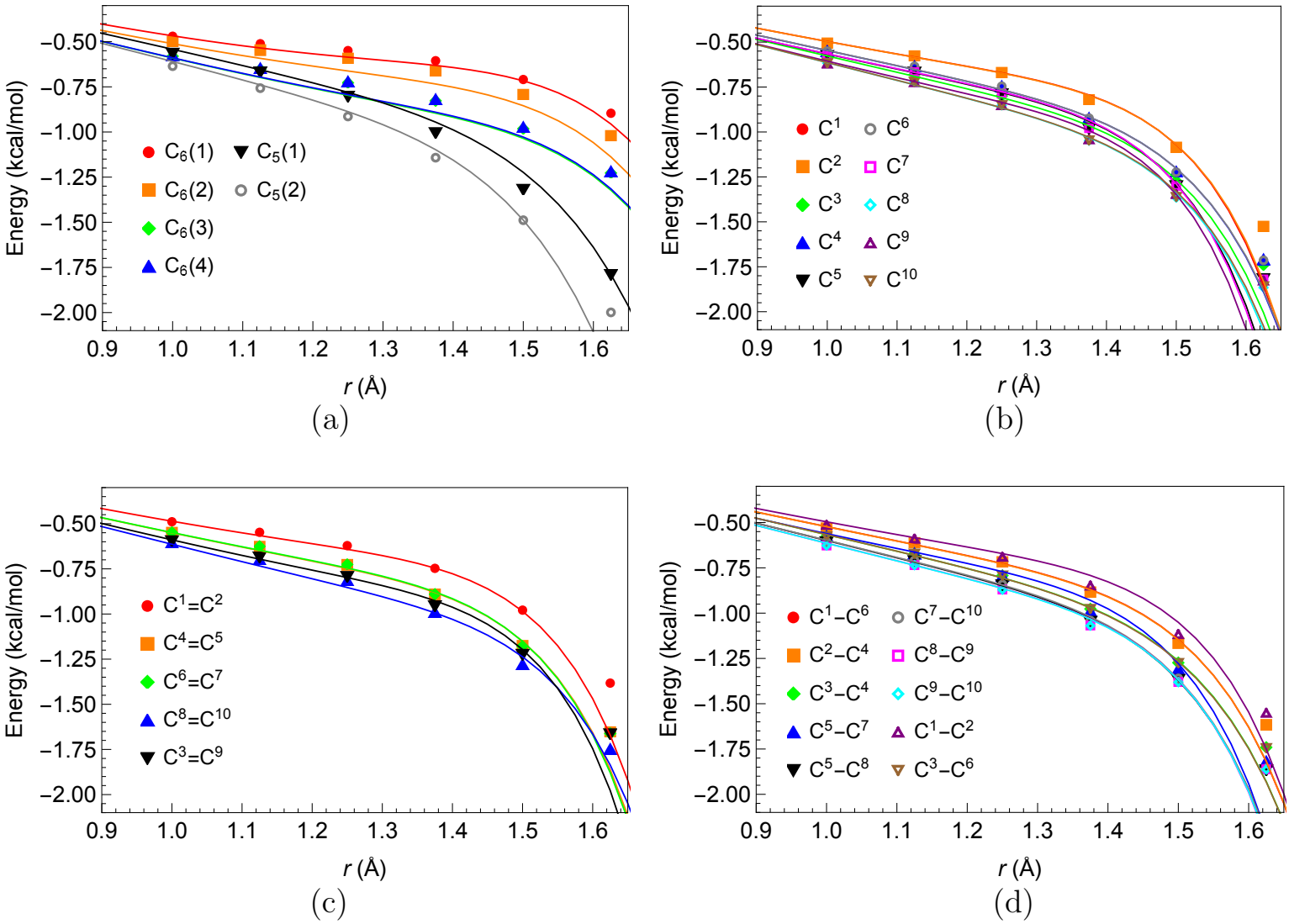

Fig. S10. Radial profiles of the dispersion energy function V_{disp} (curves) along the 31 one-dimensional rays: the rays toward (a) ring centers, (b) C atoms, (c) C=C bond centers, and (d) C−C bond centers. The symbols are the single-point calculation energies, ΔE_{disp}, which are relative to the energy at $r = 0$ Å.

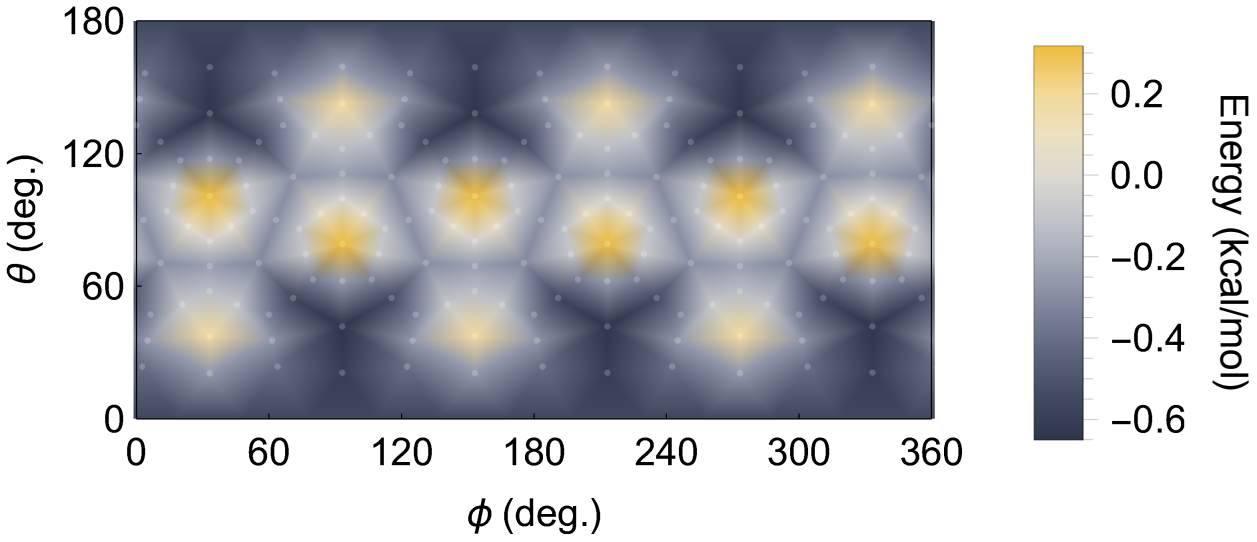

(a) Single-point calculation

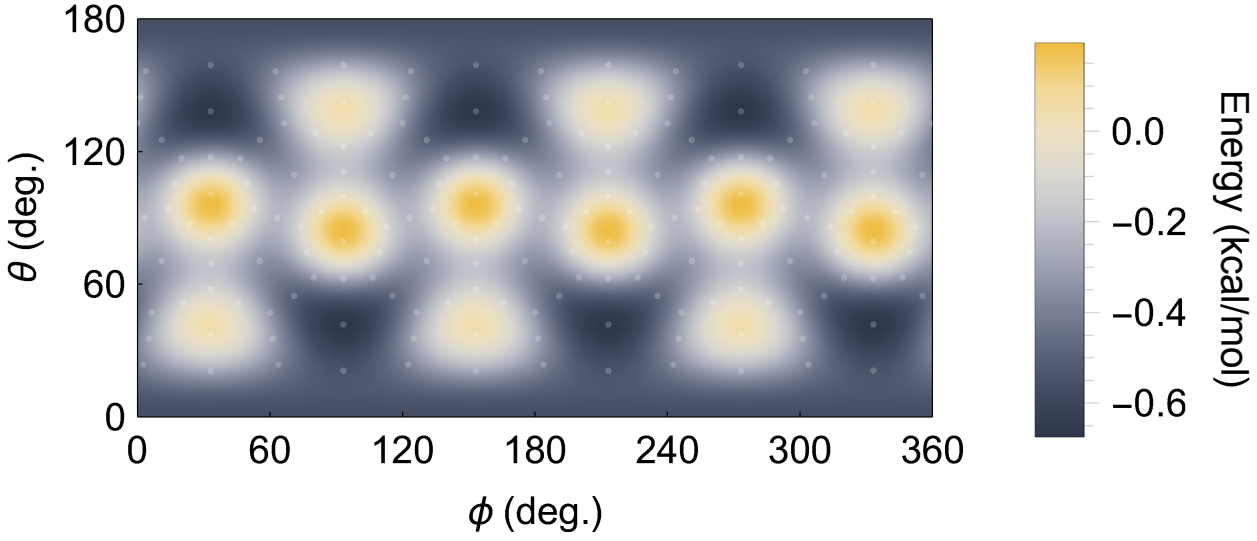

(b) Model function

Fig. S11. Polar plot of the electrostatic energy function in a spherical shell with $r = 1.375$ Å: (a) the single-point calculation data ΔE_{es} and (b) the model function V_{es}. The positions underneath the C atoms, bond centers, and ring centers, except those underneath the $C_6(1)$ centers at the two poles, are indicated by the semitransparent white points, at which single-point calculations were performed. The color map was generated by interpolating the data points by means of a Delaunay triangulation. The plot range, shown in the bar legend, was defined by using the minimum and maximum energies in the spherical shell with $r = 1.375$ Å.

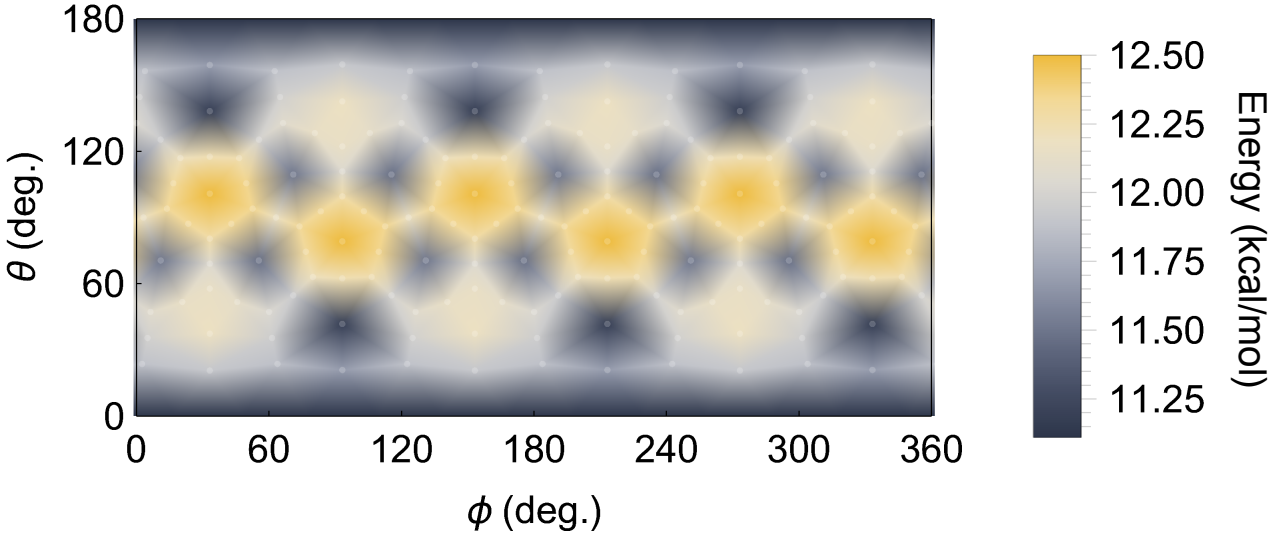

(a) Single-point calculation

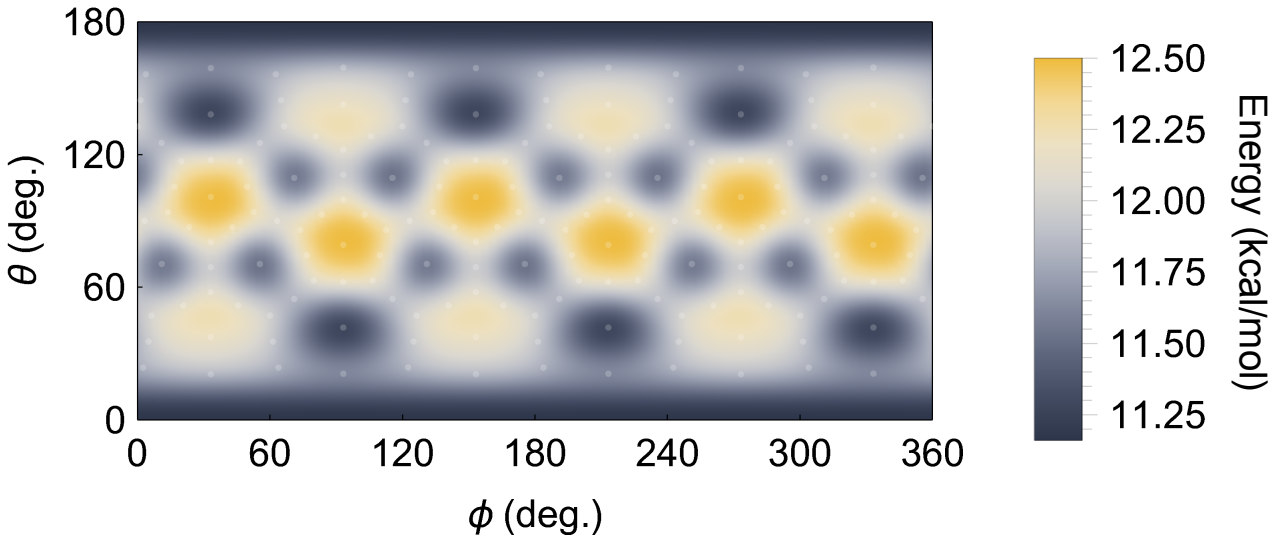

(b) Model function

Fig. S12. Polar plot of the decomposed energy function $V_{\mathrm{es+exrep}}$ in a spherical shell with $r = 1.375$ Å: (a) the single-point calculation data, $\Delta E_{\mathrm{es}} + \Delta E_{\mathrm{exrep}}$, and (b) the model function $V_{\mathrm{es+exrep}}$. The positions underneath the C atoms, bond centers, and ring centers, except those underneath the $C_6(1)$ centers at the two poles, are indicated by the semitransparent white points, at which single-point calculations were performed. The color map was generated by interpolating the data points by means of a Delaunay triangulation. The plot range, shown in the bar legend, was defined by using the minimum and maximum energies in the spherical shell with $r = 1.375$ Å.

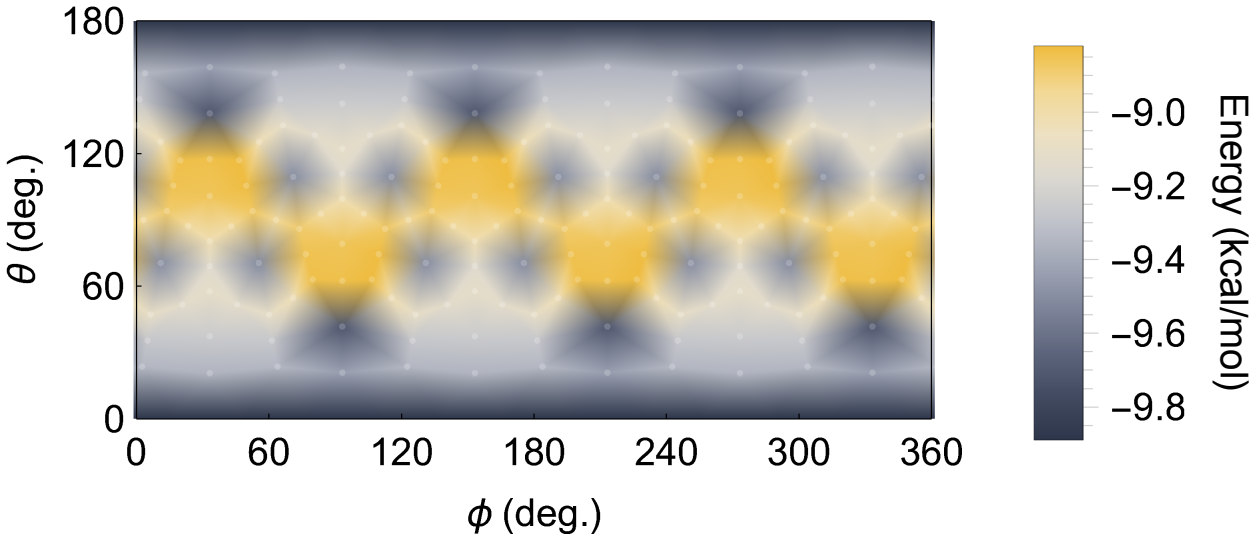

(a) Single-point calculation

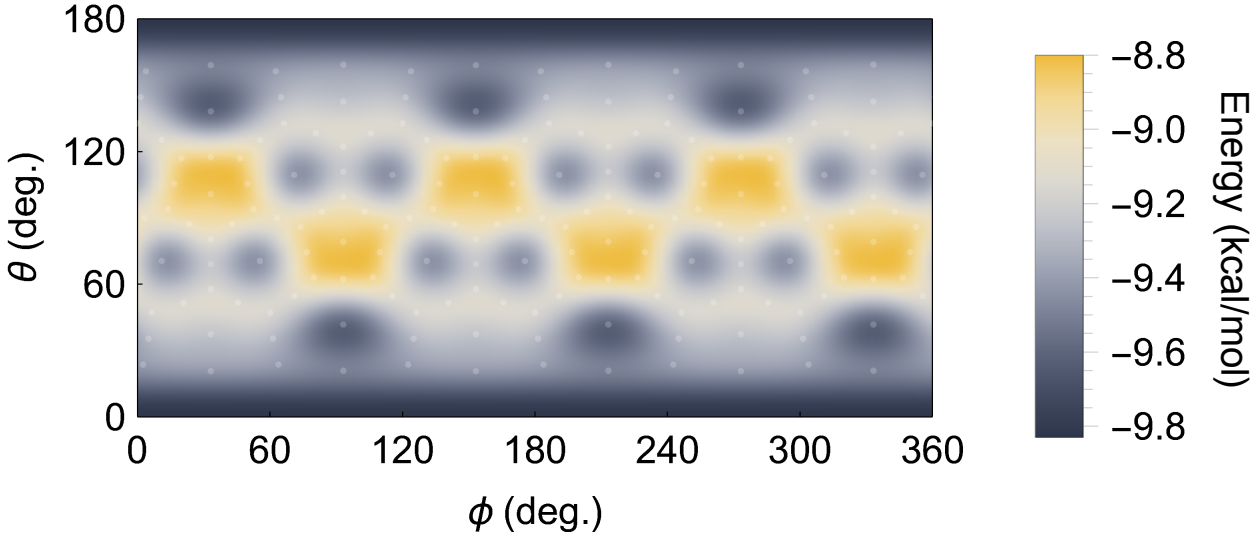

(b) Model function

Fig. S13. Polar plot of the RHF potential energy function in a spherical shell with $r = 1.375$ Å: (a) the single-point calculation data, $\Delta E_{\mathrm{es}} + \Delta E_{\mathrm{exrep}} + \Delta E_{\mathrm{pol}}$, and (b) the model function $V_{\mathrm{es+exrep+pol}}$. The positions underneath the C atoms, bond centers, and ring centers, except those underneath the $C_6(1)$ centers at the two poles, are indicated by the semitransparent white points, at which single-point calculations were performed. The color map was generated by interpolating the data points by means of a Delaunay triangulation. The plot range, shown in the bar legend, was defined by using the minimum and maximum energies in the spherical shell with $r = 1.375$ Å.

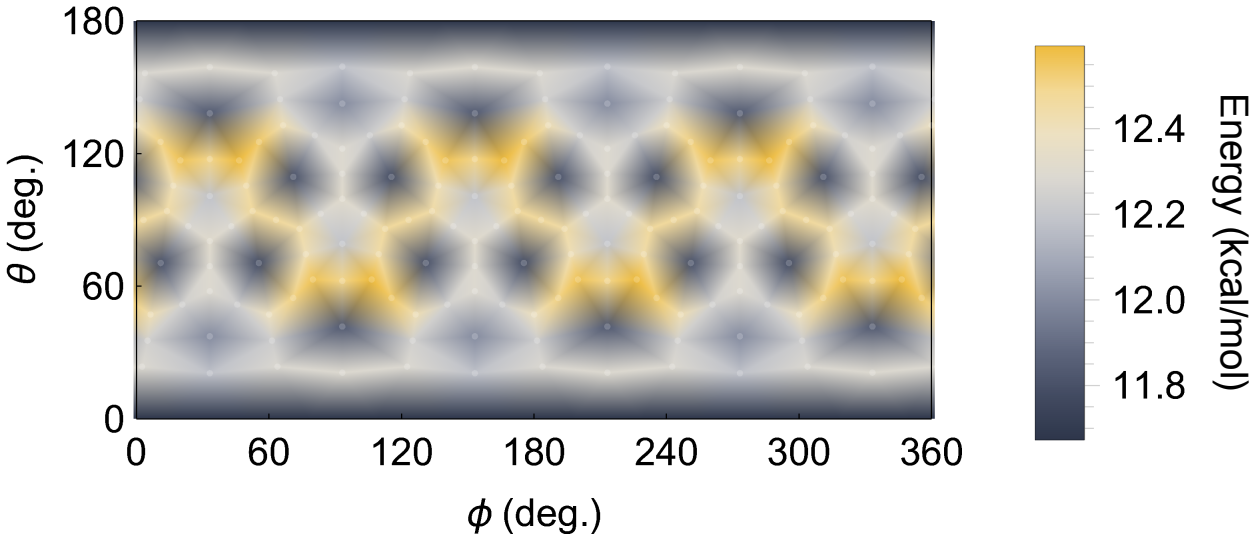

(a) Single-point calculation

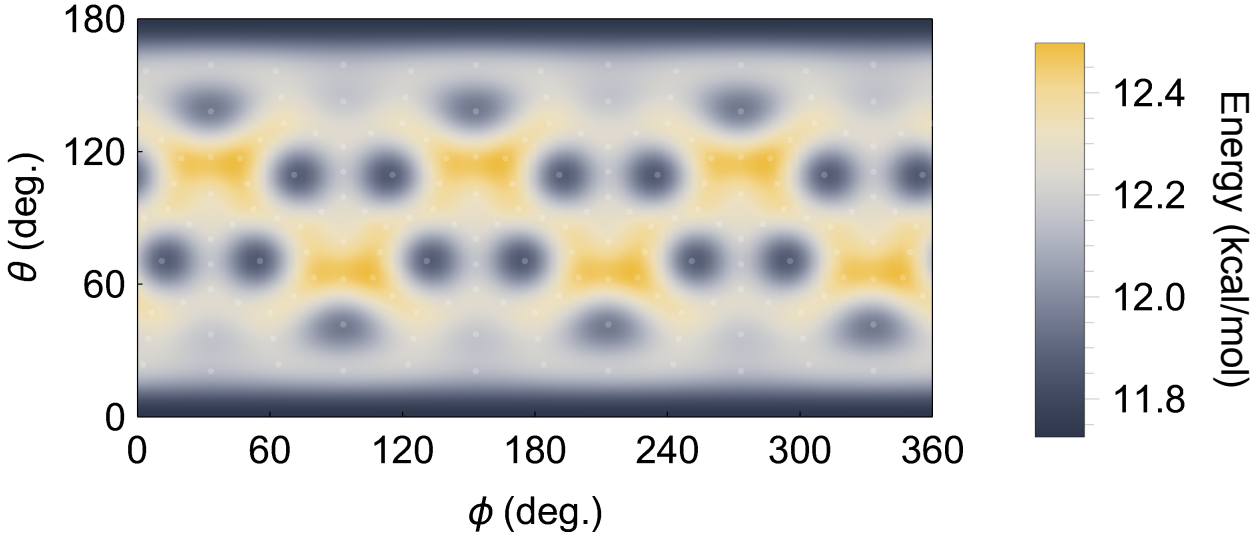

(b) Model function

Fig. S14. Polar plot of the exchange repulsion energy function in a spherical shell with r = 1.375 Å: (a) the single-point calculation data $\Delta E_{\mathrm{exrep}}$ and (b) the model function V_{exrep}. The positions underneath the C atoms, bond centers, and ring centers, except those underneath the $C_6(1)$ centers at the two poles, are indicated by the semitransparent white points, at which single-point calculations were performed. The color map was generated by interpolating the data points by means of a Delaunay triangulation. The plot range, shown in the bar legend, was defined by using the minimum and maximum energies in the spherical shell with $r = 1.375$ Å.

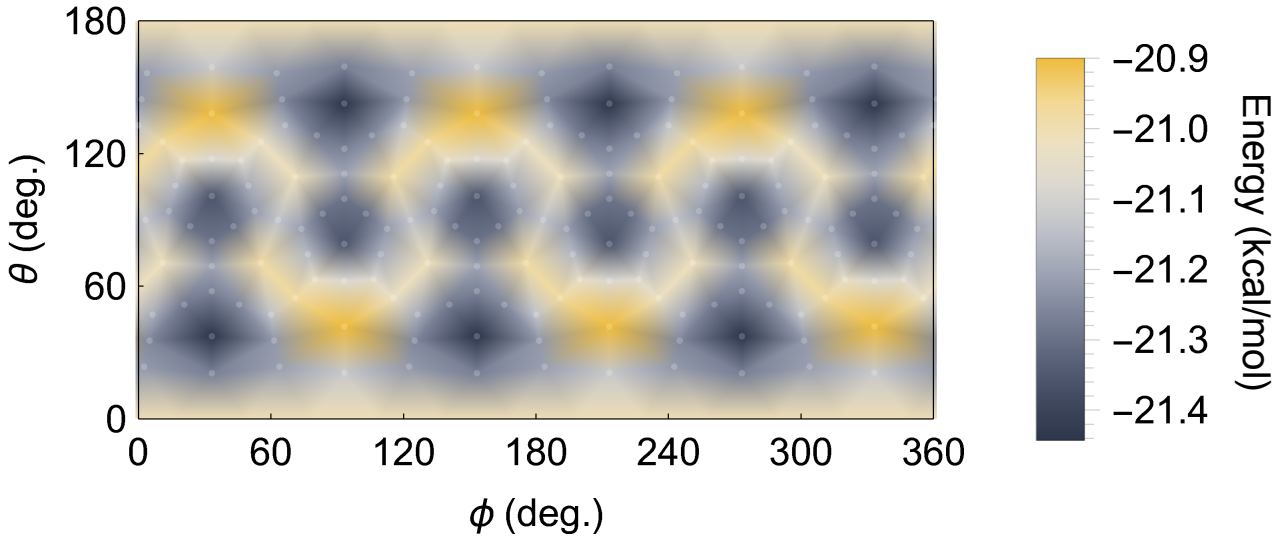

(a) Single-point calculation

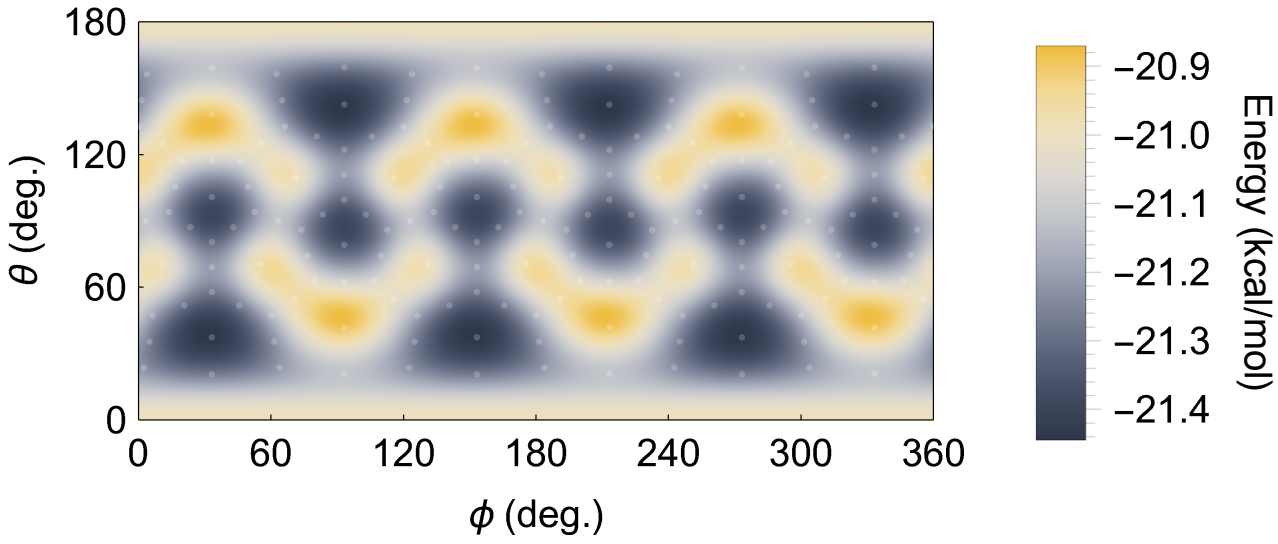

(b) Model function

Fig. S15. Polar plot of the polarization energy function in a spherical shell with $r = 1.375$ Å: (a) the single-point calculation data ΔE_{pol} and (b) the model function V_{pol}. The positions underneath the C atoms, bond centers, and ring centers, except those underneath the $C_6(1)$ centers at the two poles, are indicated by the semitransparent white points, at which single-point calculations were performed. The color map was generated by interpolating the data points by means of a Delaunay triangulation. The plot range, shown in the bar legend, was defined by using the minimum and maximum energies in the spherical shell with $r = 1.375$ Å.

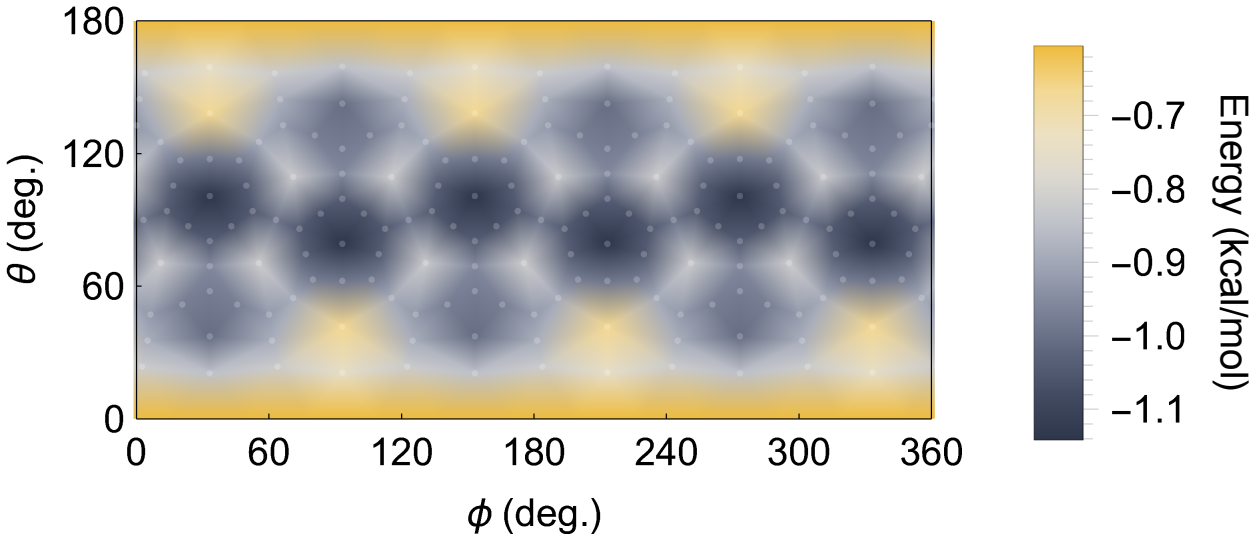

(a) Single-point calculation

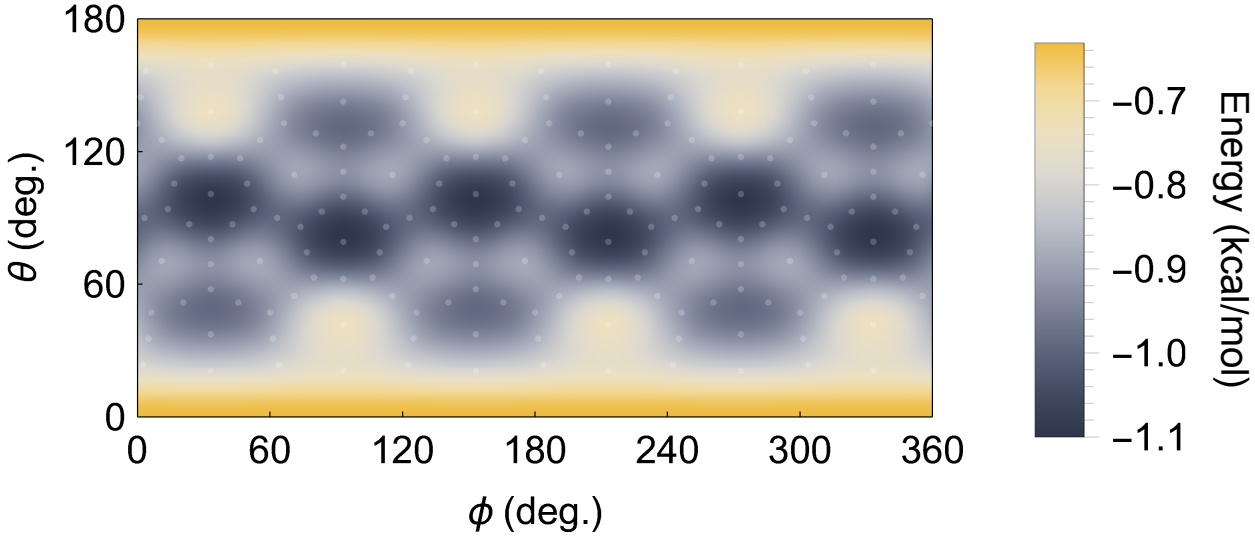

(b) Model function

Fig. S16. Polar plot of the dispersion energy function in a spherical shell with $r = 1.375$ Å: (a) the single-point calculation data ΔE_{disp} and (b) the model function V_{disp}. The positions underneath the C atoms, bond centers, and ring centers, except those underneath the $C_6(1)$ centers at the two poles, are indicated by the semitransparent white points, at which single-point calculations were performed. The color map was generated by interpolating the data points by means of a Delaunay triangulation. The plot range, shown in the bar legend, was defined by using the minimum and maximum energies in the spherical shell with $r = 1.375$ Å.

Detailed analysis of the polar plots of the interaction energy functions in Fig. 4

Figure 4a displays the polar plot of $V_{\rm es}(x, y, z)$ at $r = 1.375$ Å. The dark gray areas around the $C_6(1)$ and $C_6(2)$ wells and the medium gray areas around the $C_6(3)$ and $C_6(4)$ wells are interconnected, unlike the isolated gray spots and stripes in $V_{\rm es+exrep+pol+disp}$ (Fig. 2b). Hence, the electrostatic stabilization occurs not only underneath the C_6 centers but also underneath every C=C center between the C_6 rings. As shown in Fig. S5c, the electrostatic stabilization is large, particularly underneath the centers of the C^1=C^2, C^4=C^5, and C^6=C^7 bonds (-0.51 kcal/mol on average), which compose the $C_6(1)$ and $C_6(2)$ rings.

Figure 4b displays the polar plot of $V_{\rm exrep}(x, y, z)$ at $r = 1.375$ Å. Every U-shaped yellow highlight, discussed in the main text, extends from the outer edge of the $C_5(2)$ ring to the interspace between two of the nearby $C_6(2)$, $C_6(3)$, and $C_6(4)$ spots. Each interspace highlighted in yellow corresponds to an area underneath a C^4=C^5, C^6=C^7, or C^8=C^{10} bond (Fig. S1). This destabilization is also attributed to the short distances of the participating C atoms from the cage center; note that the $r_{\rm C}$ distances of C^4 and C^6 atoms are somewhat short (Table S2). The polar image of $V_{\rm exrep}$ in Fig. 4b resembles that of the RI-MP2 model potential, $V_{\rm es+exrep+pol+disp}$, in Fig. 2b. In both images, the dark gray spots and stripes of the C_6 wells are clearly separated from each other by the boundaries that the C=C and C−C bonds form. This is also the case with the polar images of $V_{\rm es+exrep}$ (Fig. S12) and $V_{\rm es+exrep+pol}$ (Fig. S13). These suggest that the C_6 wells of the RI-MP2 potential, $V_{\rm es+exrep+pol+disp}$, are separated chiefly due to the exchange repulsion with the C=C and C−C bonds. A noteworthy difference between the polar images of $V_{\rm exrep}$ and $V_{\rm es+exrep+pol+disp}$ is in the energy scale and sign. Since the exchange repulsion interaction is purely repulsive (Fig. S8), $V_{\rm exrep}$, unlike $V_{\rm es+exrep+pol+disp}$, is positive over the whole spherical surface with $r = 1.375$ Å.

Figure 4c displays the polar plot of $V_{\rm pol}(x, y, z)$ at $r = 1.375$ Å. The yellow areas underneath the $C_6(2)$ centers and the pale yellow ones underneath the $C_6(1)$, $C_6(3)$, and $C_6(4)$ centers are interconnected. This indicates that the polarization stabilization is small not only underneath the C_6 rings but also underneath the C=C centers.

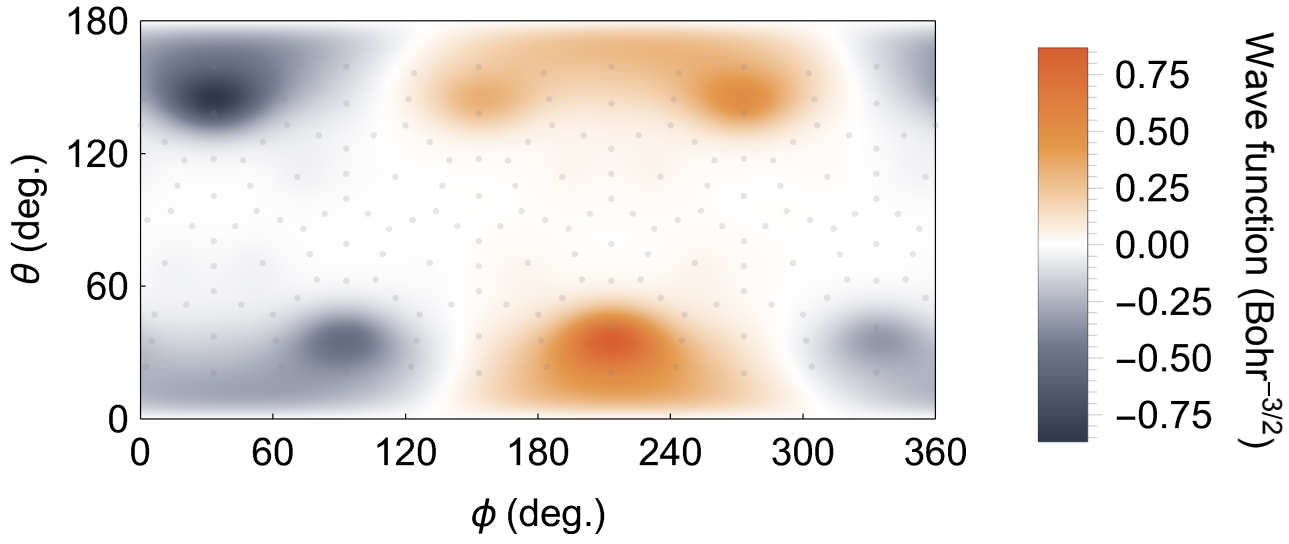

(a) E_u

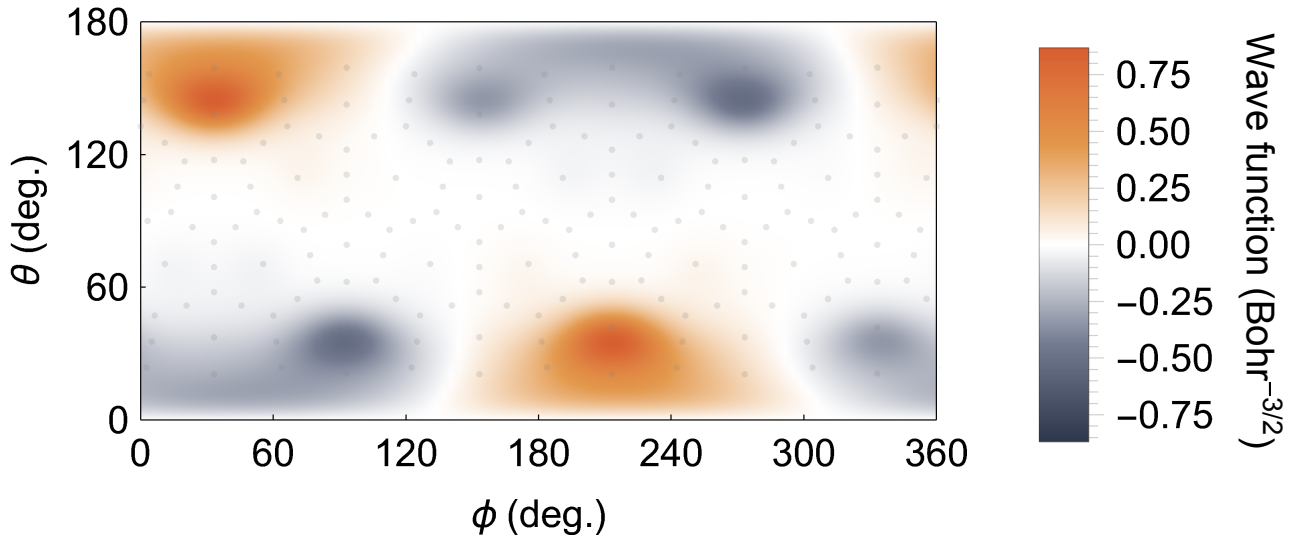

(b) E_g

Fig. S17. Polar plots of (a) an excited-state E_u wave function and (b) an excited-state E_g wave function of Li^+ in the $[Li^+@C_{60}]6PF_6^-$ model. Their degenerate counterparts are shown in Fig. 6c and d. In the polar plots, the distance from the cage center (r) is fixed at 1.375 Å. The positions underneath the C atoms, bond centers, and ring centers, except those underneath the $C_6(1)$ centers at the two poles, are indicated by the gray points.

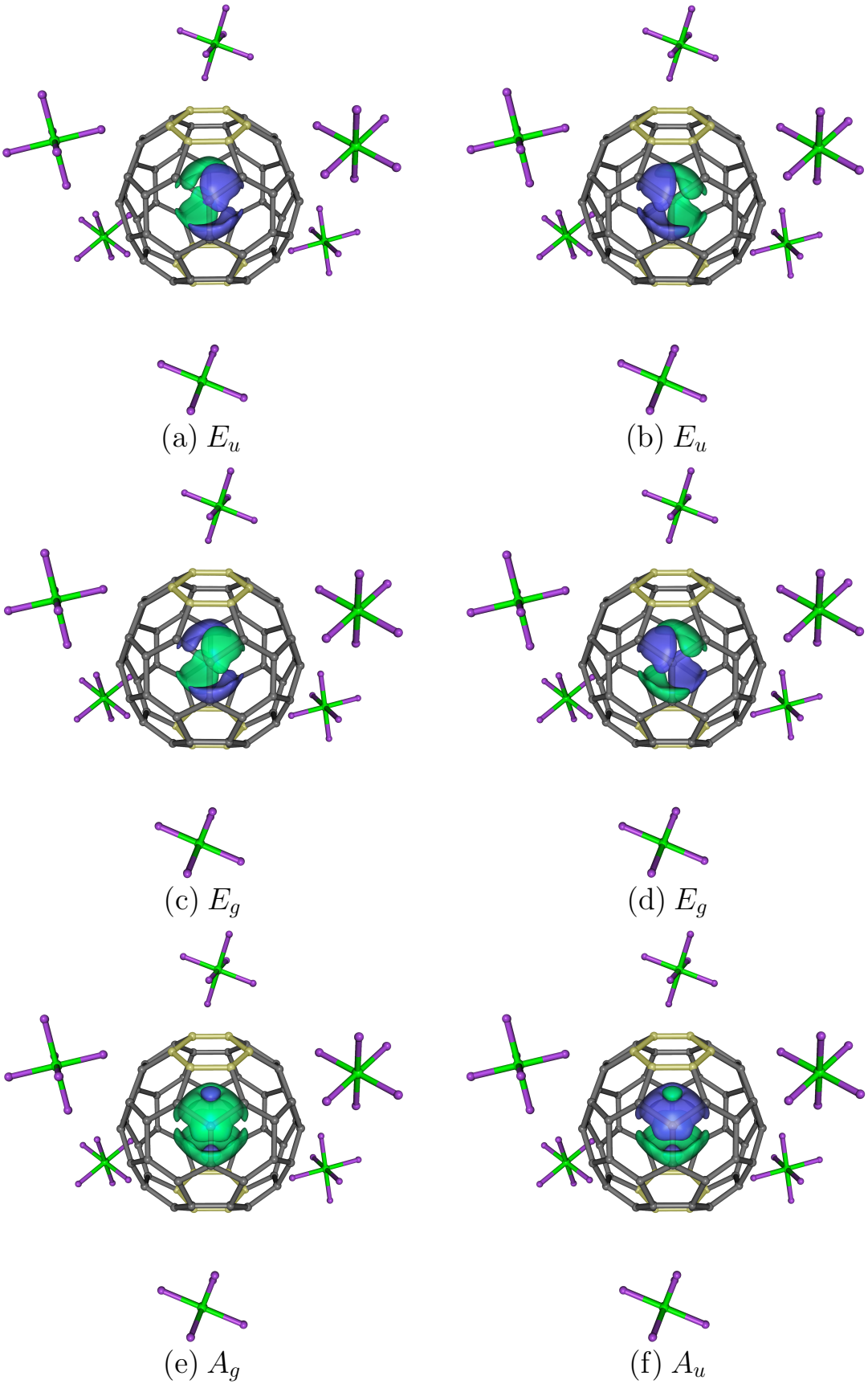

Fig. S18. Six lowest-energy excited-state nuclear wave functions of Li^+ in the $[Li^+@C_{60}]6PF_6^-$ model, which are presented in increasing energetic order. Panels (a) and (b) and panels (c) and (d) show excited-state E_u wave functions and excited-state E_g ones, respectively. Panels (e) and (f) show an excited-state A_g wave function and an excited-state A_u one, respectively. The blue and green isosurfaces in the panels were generated using the isosurface contour values of ± 0.02 $Bohr^{-3/2}$. The two $C_6(1)$ rings are indicated by the yellow highlights.